Astron. Astrophys. 326, 1195–1214 (1997)

ASTRONOMY
AND
ASTROPHYSICS

Dynamical evolution of wind-driven H II regions in strong density gradients

F. Comerón

European Southern Observatory, Karl-Schwarzschild-Strasse 2, D-85748 Garching bei München, Germany

Received 7 March 1997 / Accepted 9 June 1997

Abstract. The *champagne* model which describes the dynamical evolution of HII regions in the presence of a density discontinuity is reexamined including the effects of stellar winds. We consider stars with widely different ratios of ionizing flux to stellar wind power, as well as different distances between the star and the boundary of its parental molecular cloud. We also performed simulations with reduced cooling by suppressing thermal conduction. The evolution of the gas is followed by means of axisymmetric 2-D numerical simulations.

The hot gas generated by a shocked stellar wind produces important morphological differences with respect to the windless case: the basic one is that the dense shell of swept-up gas which surrounds the bubble of hot gas reaches velocities much higher than those of the outer boundary of the *champagne* flow in the windless case, and the volume affected by the blowout of the HII region is accordingly much greater. Instabilities in the expanding shell are likely to make the density and velocity structure of the HII region more complex.

Simulated maps of X-ray emission produced by the shocked stellar wind are presented and discussed. X-ray emission has a compact and an extended peak, both in intensity and in hardness ratio, arising from the different shock structures present inside the hot bubble. We also present maps of low frequency emission, with emphasis on the continuum emission as a tracer of emission measure and on the line-to-continuum ratio at a given frequency as a tracer of kinematic structure.

Key words: stars: early-type – ISM: bubbles; clouds; H II regions; kinematics and dynamics – hudrodynamics

1. Introduction

HII regions rarely display the spherical symmetry assumed by the standard Strömgren theory of an expanding volume of photoionized gas. Rather, density gradients between molecular clouds, where massive stars are born, and their surroundings cause large distortions in the shapes of HII regions, and flows of material towards the less dense regions (see for example Gómez et al. 1993, Wilcots 1994, Keto et al. 1995, Russeil et al. 1995, Koo et al. 1996). Such density gradients have been invoked to explain weakly collimated outflows produced by the winds of low mass stars, and were numerically modelled by Różyczka & Tenorio-Tagle 1985a, 1985b. The evolution of HII regions in the presence of density discontinuities was studied by Tenorio-Tagle and coworkers in a series of papers (Tenorio-Tagle 1979, 1982, Tenorio-Tagle & Bedijn 1982, Tenorio-Tagle et al. 1979, Bodenheimer el al. 1979) where the bases of the so-called *champagne* model was established. Some features of this model, such as the runaway expansion of an ionization front, are also reproduced in outward decaying, spherically symmetric density distributions, provided that the density gradient exceeds some critical value (Franco et al. 1990, Rodríguez- Gaspar et al. 1995). The *champagne* model achieved a remarkable success in explaining the general morphology of actual HII regions and features in their velocity fields (see review by Yorke 1986).

The *champagne* model considers photoionization by a central star as the source of energy behind the expansion. Nevertheless, it is widely recognized now that the strong stellar winds produced by the same massive stars which ionize the HII regions play a major role in the large scale shaping of the interstellar medium by generating expanding structures around them (Weaver et al. 1977, Bruhweiler et al 1980, Beltrametti et al. 1982, Tenorio-Tagle et al. 1982, Tenorio-Tagle & Bodenheimer 1988, Mac Low et al. 1989, Bisnovatyi-Kogan & Silich 1995). Although most of the energetic output of young massive stars is in the form of ultraviolet radiation, it turns out that the mechanical power contained in the stellar wind is more efficiently transferred to the surrounding gas (Dyson & Williams 1980), making the energetic output from both sources of similar importance. Visible-light photographs of HII regions often display bubble-like structures in the lower density areas reminiscent of the effects of the low density, hot gas produced by shocked stellar winds, rather than the denser gas flows expected from the *champagne* model (see e.g. photograph of NGC 6357 in Malin 1993, p. 91). Stellar winds also play a fundamental role in explaining the basic features of ultracompact HII regions (Van Buren et al. 1990; Mac Low et al. 1991; Van Buren & Mac Low

Send offprint requests to: F. Comerón

1992) and bow shocks observed ahead of runaway stars (Van Buren et al. 1995; Kaper et al. 1997). Observations carried out by the *Einstein* and *ROSAT* X-ray satellites have shown that high energy emission produced by the hot gas is ubiquitous in massive star forming regions, pervading the area occupied by the visible nebulosity (Chu & Mac Low 1990, Wang & Helfand 1991, Belloni & Mereghetti 1994; Norci & Oegelman 1995, Magnier et al. 1996; see also Chu 1994 and references therein). Modelling of the luminosity and energy distribution of high energy emission from star forming complexes shows that the combined action of supernovae and stellar winds can account for their X-ray emission (Chu & Mac Low 1990, Arthur & Henney 1996).

Actual star forming regions are far more complex than models can deal with: molecular clouds are highly inhomogeneous, their internal dynamics is greatly influenced by turbulent motions and magnetic fields, and massive stars tend to form in aggregates rather than in isolation. However, the *champagne* model is still useful in establishing a simple framework where the essential ingredients necessary to understand the dynamics of the interstellar medium around newly formed massive stars can be taken into account: large density discontinuities and the dominant energy sources from the central object. Therefore, both theoretical and observational evidence call for a reexamination of the *champagne* model, taking into consideration both photoionization *and* stellar winds (García-Segura & Franco 1996). This is the subject of this paper: we present the results of axisymmetric 2-D numerical simulations of a HII region expansion whose energy input includes both a stellar wind and photoionization. A comparison with photoionization-alone models is made.

We will focus on the large scale morphological and kinematic properties of the region, showing the distribution of the most relevant physical quantities. We have also produced simulated maps of X-ray emission in two broad bands, and maps of long wavelength recombination line to free-free continuum ratio, which can be useful for the interpretation of observations. Given the large range of geometrical and physical input parameters defining the scenario studied here, we do not intend to be exhaustive in exploring all the possible configurations; rather, we will concentrate on the dominant features of the blowout phase, leaving the application to specific sets of parameters to further studies of particular objects of interest.

In the next section, we describe the initial conditions assumed for the cloud and intercloud medium, as well as an outline of the numerical methods employed for simulating the expansion, and the relevant parameters of the exciting stars. Sect. 3 presents and describes the results obtained for the evolution of regions containing different stars at different distances from the cloud-intercloud interface, including the simulated maps at different wavelengths. Simulations without stellar wind or without thermal conduction are presented there as well for comparison. Our conclusions are summarized in Sect. 4.

2. Initial conditions and numerical methods

In all the simulations presented in this paper, we will assume that the star is initially embedded in a dense cloud with $n_H = 10^3$ cm^{-3} and $T = 29$ K, in pressure equilibrium with a neutral diffuse medium with $n_H = 3.4$ cm^{-3} and $T = 8500$ K. Such conditions may be commonly expected in molecular clouds (Blitz 1993). The distance from the star to the edge of the cloud is a free parameter expressed in multiples of the Strömgren radius in the dense medium. Heating of the cloud and intercloud medium is assumed to be proportional to the density in regions shielded from the ultraviolet radiation of the star. We have taken the expressions for cosmic ray heating given by Black 1987, but multiplied by a scaling factor so that the intercloud medium is thermally stable at the assigned temperature: a phase transition to a cold phase takes place when the density exceeds $n_H = 10$ cm^{-3}. Although this is an arbitrary choice, the only relevant role played by such heating is to keep the temperatures of the unperturbed cloud and intercloud media at their initial values, which are little sensitive to the actual value of the heating rate. In regions where the Lyman continuum flux of the star is nonzero, we assume a blackbody spectral energy distribution of the ionizing radiation and a cross section for ultraviolet photon absorption by hydrogen atoms proportional to ν^{-3} (Spitzer 1978), with the excess photon energy going into heating of the gas. To simplify radiative transfer calculations, we neglect the hardening of the ultraviolet flux with increasing column density to the ionizing source. Only hydrogen photoionization is considered. Further simplifications include the on-the-spot and radial flux approximations (Bodenheimer et al. 1979, García-Segura & Franco 1996). Dust absorption is assumed to be proportional to the density, adopting an averaged opacity of $\kappa = 200$ cm^2 g^{-1} in the ultraviolet (Yorke et al. 1984). The transfer equation of ionizing radiation is thus

$$\frac{\partial F_{UV}}{\partial r} = -\beta n_H^2 (x_i - x_H) - 1.4 m_H n_H \kappa F_{UV} - \frac{2F_{UV}}{r} \quad (1)$$

where F_{UV} is the ionizing flux, β is the recombination coefficient excluding the ground level, $x_i = (n_e/n_H)$ is the ionization fraction (n_e = electron density, n_H = proton density), x_m is the contribution of electrons from ionized metallic species to the ionization fraction (set to $x_m = 3 \cdot 10^4$), and r is the distance to the ionizing star. The numerical integration of Eq. (1) is carried out proceeding outwards from the star, making

$$F_{UV} = F_{UV_0} - \mathscr{A}(F_{UV_0})\Delta r \quad (2)$$

where $\mathscr{A}(F_{UV_0})$ is the right-hand term of Eq. (1), and F_{UV_0} is the ionizing flux at $r_0 = r - \Delta r$. F_{UV_0} is interpolated from the fluxes at the positions of the nearest cells j, k as

$$F_{UV_0} = \frac{1}{2r_0^2}(r_j^2 F_{UV_j} + r_k^2 F_{UV_k}) \quad (3)$$

The ionization fraction x_i is set at each point at the equilibrium value, given by the balance between photoionization, collisional ionization, and radiative recombination to levels other than the ground.

Cooling of the cool and warm gas is mainly by collisional excitation of fine structure metastable levels of neutral and ionized metals, for which expressions are taken from Dalgarno & McCray 1972. Cooling by collisional ionization and radiative recombination of hydrogen is also included, with relevant rate coefficients from Spitzer 1978. For $T > 10^4$ K, an interpolation of the cooling curve of Gaetz & Salpeter 1983 is used. No molecular gas has been explicitly considered, as this should be photodissociated by the stellar radiation with wavelengths longwards from the Lyman limit. Such radiation should also produce an increase in the temperature of the gas, which we have neglected. However, we have checked that this warming does not have any noticeable dynamical consequences on the process studied here.

The numerical simulations are carried out by means of a two-dimensional explicit Eulerian hydrodynamic code, using cylindrical coordinates on a computational grid of 200×400 cells. The hydrodynamic equations in cylindrical coordinates are used in the more convenient form for numerical integration:

$$\frac{\partial \rho}{\partial t} = -\frac{\partial(\rho u)}{\partial z} - \frac{\partial(\rho v)}{\partial x} - \frac{\rho v}{x} \tag{4}$$

$$\frac{\partial u}{\partial t} = \frac{1}{\rho}\frac{\partial p}{\partial z} - \frac{u}{\rho}\left(\frac{\partial(\rho u)}{\partial z} - u\frac{\partial \rho}{\partial z}\right) - \frac{v}{\rho}\left(\frac{\partial(\rho u)}{\partial x} - u\frac{\partial \rho}{\partial x}\right) \tag{5}$$

$$\frac{\partial v}{\partial t} = \frac{1}{\rho}\frac{\partial p}{\partial x} - \frac{v}{\rho}\left(\frac{\partial(\rho v)}{\partial x} - v\frac{\partial \rho}{\partial x}\right) - \frac{u}{\rho}\left(\frac{\partial(\rho v)}{\partial z} - v\frac{\partial \rho}{\partial z}\right) \tag{6}$$

$$\frac{\partial e}{\partial t} = -\frac{5}{3}\frac{e}{\rho}\left(\frac{\partial(\rho u)}{\partial z} - u\frac{\partial \rho}{\partial z}\right) - \frac{5}{3}\frac{e}{\rho}\left(\frac{\partial(\rho v)}{\partial x} - v\frac{\partial \rho}{\partial x}\right) - u\frac{\partial e}{\partial z} - v\frac{\partial e}{\partial x} - \frac{5}{3}\frac{ev}{x} \tag{7}$$

where z and x are respectively the axial and radial coordinates; ρ and e are the densities of matter and internal energy; p is the pressure ($p = 2/3\ e$); and u and v are the axial and radial components of the velocity.

The effect of a spherically symmetric stellar wind with mass loss rate $\dot{M}_w$ and terminal velocity v_∞ has been simulated in most cases by assuming a wind free-flowing region, defined by the computational cells lying at a radius less than ten times the cell size from the star. At the centers of these shells, the density is set to the corresponding value for a free-flowing wind, $\rho = \dot{M}_w/(4\pi r^2 v_\infty)$. However, it is found sometimes that, when rescaling the computational grid to model the late stages of expansion (increasing the cell size), the shock front which defines the outer boundary of the free flowing wind lies inside the new ten cell-size radius from the star. In these cases, the effect of the stellar wind is simulated instead by assuming that all the kinetic energy of the wind is transformed into thermal energy in the vicinity of the star; the momentum and energy input is then simulated by increasing the material and energy densities in the cells surrounding the star (again within a ten cell-size radius) at a rate $\dot{\rho}_*$ and $\dot{e}_*$, respectively, so that their integrated values over the sphere volume equal $\dot{M}_w$ and $\frac{1}{2}\dot{M}_w v_\infty^2$. This is taken into account when numerically integrating the hydrodynamic equations by adding the source terms $+\dot{\rho}_*$, $-(\dot{\rho}_*/\rho)u$, $-(\dot{\rho}_*/\rho)v$, and $\dot{e}_*$ to Eqs. (4), (5), (6), and (7), respectively.

The particular form of Eqs. (4-7) is motivated by the convenience of expressing partial derivatives in a form suitable for finite difference equations, as stressed by Monaghan 1992; in our numerical scheme, the quantities assumed to vary linearly from cell to cell are the density of matter ρ and the components of the momentum density ρu, ρv, while we approximate the derivative of the energy density as

$$\frac{\partial e}{\partial l} \simeq \frac{\Delta e}{\Delta l} - \frac{1}{l}(\rho_{+l}(V_{+l} - V_0)^2 - \rho_{-l}(V_0 - V_{-l})^2) \tag{8}$$

where l is one of the cylindrical coordinates x, z, and V is the component of the velocity in the direction of that coordinate. The subindex 0 denotes the local value of a quantity, and $+l$ and $-l$ the values one computational cell ahead and behind in the l direction, respectively. Assuming this form of the energy density gradient naturally introduces an artificial viscosity term in Eqs. (5), (6), and (7).

The inclusion in our calculations of high energy, low density gas enables the appearance of large accelerations in very short timescales due to its small inertia, especially near its interfaces with the dense gas. Updating the values of ρ, u, v, and e by simply multiplying the right-hand sides of Eqs. (4)-(7) by Δt would then require exceedingly small time steps to avoid rapid oscillations in the direction of motion of small regions of the hot gas. This is particularly motivated by the dependence of the artificial viscosity term on the square of the velocity. To avoid this, Eqs. (4) to (7) may be written in the following form for a given computational cell:

$$\frac{\partial A}{\partial t} = \alpha A + \beta \tag{9}$$

where A is any of the quantities appearing in the left-hand sides of Eqs. (4)-(7); α and β contain combinations of values of the other variables and A in that cell and in neighbouring ones. Both α and β are assumed to remain constant along one computation step Δt, so that numerical integration of (4)-(7) implies solving equations of the type

$$A(t + \Delta t) = \frac{1}{\alpha}[(\alpha A(t) + \beta)\ \mathrm{e}^{\alpha \Delta t} - \beta] \tag{10}$$

The value of Δt is then given by the allowed variation in A in a single computational step, together with the usual Courant condition (e.g. Arthur & Henney 1996).

After explicitly calculating the hydrodynamic evolution of the physical quantities of the fluid in a computational step, corrections are made on the energy density by multiplying the rates of heating and radiative losses by Δt. We also include the rate of energy exchange by thermal conduction between adjacent cells, for which we adopt the classical expression for unsaturated heat flux (Cowie & McKee 1977). The heat conduction flux between each pair of adjacent cells is calculated at their midpoint, and the

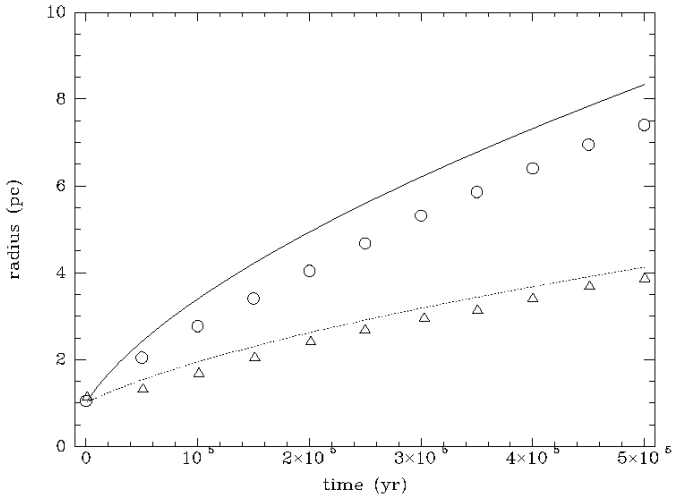

Fig. 1. Comparison between analytical solutions and numerical simulations of the time evolution of the radius of a wind-blown bubble and a Strömgren sphere. In both cases, the initial radius is the Strömgren radius. The case of the wind bubble is represented by the solid line (analytical approximation) and open circles (numerical solution). The expansion of the Strömgren sphere is replresented by the dashed line (analytical approximation) and open triangles (numerical solution).

value of $\nabla^2(T^{7/2})$ is estimated assuming that both matter and energy density vary linearly between them. The corrections are then recomputed with the new values of the energy density so that, if the sign of the correction is found to change, the equilibrium value of the energy density is adopted. Further corrections to the energy density are made as required after recomputing the ionizing flux distribution across the computational grid.

We have tested the reliability of the numerical methods employed here by simulating the time evolution of two cases with well-known analytical solutions: the expansion of a shell surrounding a bubble with constant injection of energy inside it, and the expansion of a Strömgren sphere powered only by photoionization, both in a homogeneous, low pressure medium. Simple analytical approximations to these problems exist (e.g. Dyson & Williams 1980, Shu 1993) which give the evolution of the radius, and other physical quantities, as a function of time. The results of one such comparison are shown in Fig. 1: the input parameters are those of a O4 star (see Sect. 2.1), embedded in a uniform medium of density n_H = 1000 cm^{-3}, and the evolution is followed for $5 \cdot 10^5$ yr, comparable to the span of our simulations. In the windless case, the initial radius is the Strömgren radius, with the velocity set to zero everywhere. For the case with wind, the simulation is started at the time when the expanding bubble reaches the Strömgren radius, with the velocity of the swept-up shell given by the analytical approximation discussed in Sect. 2.2.

An acceptable agreement is found between the numerical solutions and the behaviour expected from the analytical approximations. In particular, at large times, when the initial transients have died out, the exponents of the power laws describing the dependence of the radius with time are very similar in both the numerical and analytical evolutions. The lag between the analytical and numerical evolutions in the case of the Strömgren sphere can be explained by the assumed zero expansion velocity at the start of the simulations, which assumes an ideal, instantaneous transition from the formation to the expansion phase; otherwise, the $R \propto (1 + At)^{4/7}$ expansion law is very well reproduced. It is not possible to perform in a similar way a direct comparison between the predicted and simulated pressures, as the analytical approach assumes a uniform pressure inside the HII region which does not correspond to the reality. However, the pressure at the end of our simulations just inside the ionization front is 10 % above the pressure predicted by the analytical approximation, and slowly falls inwards, as expected from qualitative considerations.

Concerning the case with stellar wind, the largest deviations from the analytical solution appear at the initial stages, in which the radius of the shell (defined numerically as the position of the density maximum as one proceeds away from the shell) grows more slowly than expected. We can identify two reasons for this behavior: first, the shell surrounding the bubble is very thin at the start of the simulation, and as it is evolved in time it spreads over a few cells and the maximum is slightly shifted towards the inside. Another reason seems to have to do with the fact that the gas in the bubble is initially assumed to be at rest, and large, chaotic motions induced by the bubble expansion quickly appear. A parto of the energy contents of the bubble may thus be expected to be spent in setting the hot gas in motion at the start of the simulations, rather than in producing work by expansion of the shell against the ambient medium. Nevertheless, this deviation does not last for long, and after less than 10^5 yr the bubble expansion closely follows the predicted $t^{0.6}$ law (see Sect. 2.2). The lag between the numerical and analytical solutions remains at a constant value thereafter, and the relative difference accordingly decreases with time; at the end of the $5 \cdot 10^5$ yr period covered by the simulation, the numerically found value of the radius is slightly over 90 % of the analytical one.

Table 1. Adopted stellar parameters

type	S_{UV} (s^{-1})	T_{eff} (K)	$\dot{M}_w$ (M$_\odot$ yr^{-1})	v_∞ (km s^{-1})
O4	$8.5 \cdot 10^{49}$	50,000	$7.0 \cdot 10^{-6}$	3,250
B0	$2.3 \cdot 10^{47}$	30,900	$2.5 \cdot 10^{-8}$	2,900

2.1. Stellar parameters

In the present paper, we will focus our discussion on the effects caused by two types of star with very different ratios of ultraviolet luminosity to wind mechanical power, namely an O4 star and a B0 star. The input parameters used in the simulations for these two kinds of star are given in Table 1.

The stellar parameters relevant to the problem under consideration are the ultraviolet flux of the star shortwards from the Lyman limit S_{UV} (expressed here in photons per second), the effective stellar temperature T_{eff}, the mass loss rate $\dot{M}_w$, and the terminal wind velocity v_∞. For the Lyman continuum flux, we have used the values tabulated by Hollenbach et al. 1994 (based on stellar models by Maeder & Meynet 1987), while the stellar wind parameters have been obtained from Leitherer et al. 1992, using zero-age main sequence mass-luminosity relations from Schaller et al. 1992. We have used wind parameters closer to the actual observations as presented by Leitherer et al. 1992 rather than the analytical expressions derived by them, which provide a good fit to the most massive end but are inappropriate for the B0 star.

2.2. Early evolution and initial conditions

Very soon after a star has formed, the ionized sphere around it reaches a radius close to the Strömgren radius R_S. This happens in a time much shorter than the expansion timescale of the Strömgren sphere (Dyson & Williams 1980). The stellar wind-blown bubble thus drives a shock and forms a dense shell of ionized gas inside the Strömgren sphere. The high density of the shocked shell increases the recombination rate inside it, thus reducing the flux of photons available to keep the outer HII region ionized, and eventually it grows thick enough so as to trap all the ionizing flux from the star. To calculate the conditions under which this happens, we use the expressions for the expansion of stellar wind-driven bubbles (Weaver et al. 1977), plus the strong shock approximation. The radius of the bubble, r_b, at time t is

$$r_b = 0.763(\frac{E_*}{\rho_0})^{1/5}\ t^{3/5} \tag{11}$$

where $E_* = \frac{1}{2}\dot{M}_w v_\infty^2$ is the mechanical power of the stellar wind and ρ_0 ($= 1.4 m_H n_{H0}$) is the density of the medium in which the bubble expands. The ionization front gets trapped in the expanding shell when the condition

$$S_{UV} = \frac{4}{3}\pi r_b^3 n_{H0} n_{Hs} \beta_2 \tag{12}$$

is fulfilled: n_{H0} is the density of the unperturbed medium outer to the shell, n_{Hs} is the density of the shocked gas in the shell, and β_2 is the total recombination rate excluding recombinations to the ground level. In this expression, we neglect dust absorption and recombinations inside the hot, low density gas of the bubble, and take the mass of the shell $4\pi r_b^2 \Delta r_b n_{Hs}$ to be the same as the mass originally inside the sphere of radius r_b, thus assuming that only a small fraction of the shell has evaporated by conduction. The value of n_{Hs} is estimated from the strong shock approximation, $n_{Hs} = (v_b^2/c_i^2) n_{H0}$, where c_i is the sound speed in the ionized surrounding gas. Using Eq. (11) to obtain v_b as the time derivative of r_b,

$$n_{Hs} = 0.210\frac{n_{H0}}{c_i^2}(\frac{E_*}{\rho_0})^{2/5}\ t^{-4/5} \tag{13}$$

Combining this with Eqs. (11) and (12) gives us the time t_{trap} when Eq. (12) is fulfilled:

$$t_{trap} = 2.567\frac{\mu m_H c_i^2}{\beta_2}\frac{S_{UV}}{E_* n_{H0}} \tag{14}$$

It is useful to relate the characteristic quantities of the bubble at the trapping of the ionization front to quantities associated to the expansion of the classical Strömgren sphere or to the unperturbed surrounding medium. In this way, using the values of the Strömgren sphere radius

$$R_S = 0.620\frac{S_{UV}^{1/3}}{n_{H0}^{2/3}\beta_2^{1/3}} \tag{15}$$

and the expansion timescale of the Strömgren sphere defined as

$$t_s = \frac{R_s}{c_i} \tag{16}$$

the ratios of the bubble expansion velocity to the ionized gas sound speed (v_b/c_i), the bubble radius to the Strömgren radius (r_b/R_s), the trapping time to the expansion time of the Strömgren sphere (t_{trap}/t_s) and the pressure inside the bubble to the pressure in the Strömgren sphere (p_b/p_{ext}) take the following simple forms:

$$\frac{v_b}{c_i} = 0.31\xi^{-1} \tag{17}$$

$$\frac{r_b}{R_s} = 2.17\xi^{2/3} \tag{18}$$

$$\frac{t_{trap}}{t_s} = 4.14\xi^{5/3} \tag{19}$$

$$\frac{p_b}{p_{ext}} = 0.07\xi^{-2} \tag{20}$$

where

$$\xi = \left[(\frac{\mu m_H c_i^3}{\beta_2^{2/3}})^3(\frac{S_{UV}^2}{E_*^3 n_{H0}})\right]^{1/5} \tag{21}$$

For the stellar parameters listed in Table 1 and the adopted density of the molecular cloud, we obtain $\xi = 0.015$ for an O4 star, and $\xi = 0.054$ for a B0 star. Consequently, $r_b/R_s \simeq 0.13$ for a O4 star and 0.31 for a B0 star, this is, the trapping happens when the bubble is still inside the initial Strömgren sphere. Moreover, $t_{trap}/t_s \simeq 0.004$ for the O4 star and 0.03 for the B0 star, meaning that the Strömgren sphere has not had time to expand significantly before the trapping of the ionization front in the expanding shell. Finally, the expansion of the shell takes place at $v_b/c_i \simeq 20$ for the O4 star and 5.7 for the B0 star, thus justifying the strong shock approximation to the shell expansion.

Once the ionization front becomes trapped in the expanding shell, the material in the initial HII region outside it recombines in a time $t_{rec} \sim (\beta_2 n_{H0})^{-1}$, which is only ~ 100 years in such a dense medium. Further expansion of the shell therefore takes place in a neutral medium, and the structure of the HII region is

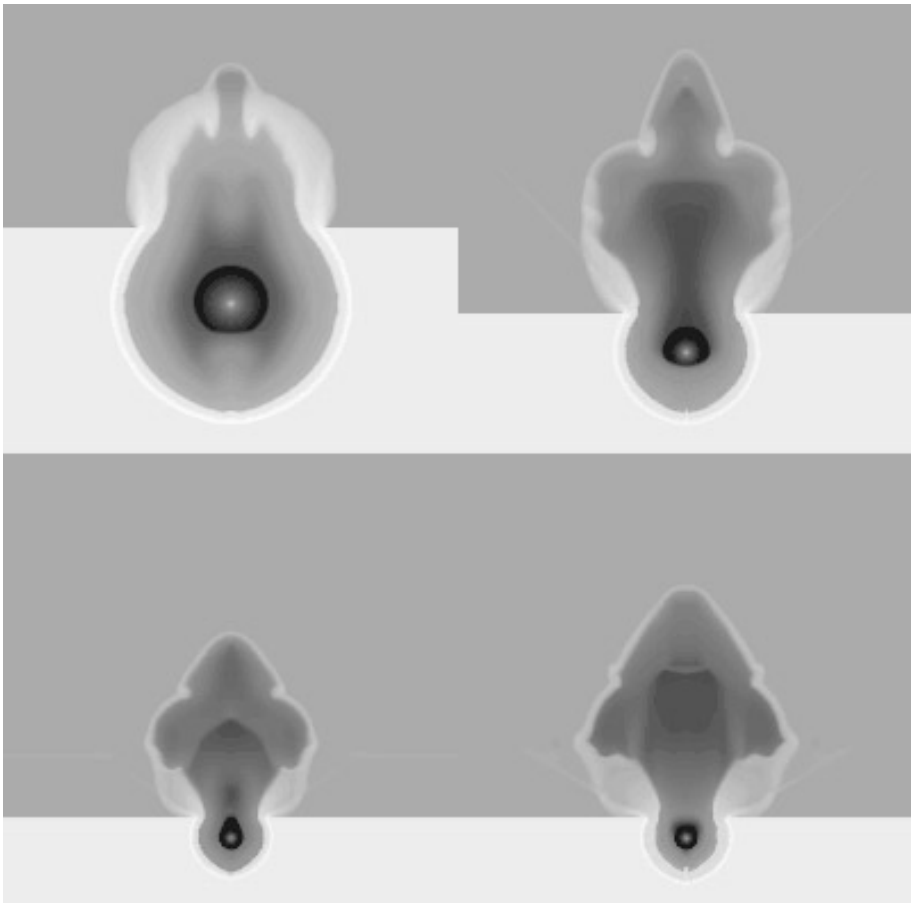

Fig. 2. Evolution of the density in the computational plane for a O4 star located 1.5 Strömgren radii from the cloud boundary. The frames correspond to the evolution $5 \cdot 10^4$, $1 \cdot 10^5$, $1.5 \cdot 10^5$, and $2 \cdot 10^5$ years after blowout. The initial size of the computational grid (upper left frame) is 9.08 pc x 9.08 pc. The computational grid has been upscaled by a factor of 2 between the first and the second frame, and again between the second and the third frame. See Sect. 3.1.1 for a detailed explanation of the different features appearing in these frames.

as depicted in Weaver et al. 1977: proceeding outwards from the star, one finds successively layers of free-flowing wind, shocked wind, dense ionized gas, shocked neutral gas shielded from the UV radiation of the star by the HII layer, and finally the neutral outer medium.

We start our simulations at the time when the expanding bubble reaches the cloud-intercloud interface, using as initial values for the variables those derived from the analytical solution to the early stages of the expansion as outlined above. The dense shell containing the HII region is assumed to be totally ionized, due to the impossibility of resolving the very thin layer of shocked neutral gas surrounding it in our computational grid; this is an acceptable approximation, as long as the surface density of the shell is dominated by the ionized component. For the interior structure of the bubble, we integrate the evaporation rate due to thermal conduction as a function of time using the analytic expressions of the radius and internal pressure from Weaver et al. 1977. In this way, one can obtain an analytic expression for the average density and temperature as a function of time, whose corresponding expressions can be found, for instance, in Shull & Saken 1995. The evaporated mass is found to be only a small fraction of the swept-up mass building up the shell, as assumed above, while an estimate of the radiative losses inside the bubble shows that in general they are small during its early evolution. The initial distributions of density and temperature are then found by assuming conductive equilibrium inside an isobaric bubble (Weaver et al. 1977, Mac Low & McCray 1988, Shull & Saken 1995). Nevertheless, this configuration is changed by the combined action of shell expansion and mechanical power injection from the central star very soon after the start of the numerical simulation.

The distance of the star to the cloud-intercloud interface is a free parameter of our simulations, which we express as a multiple d of R_S. We find it convenient to use a length of $6dR_S$ and $3dR_S$ in the z and x directions respectively as the initial size of the computational grid, with the cloud-intercloud interface located at the middle of the grid. The grid is scaled up, and the center repositioned along the axis of symmetry, when the expanding HII region approaches its boundaries.

3. Results and discussion

3.1. Dynamical evolution

In this section we focus on the aspects related to the dynamical evolution of the gas affected by the expansion of the HII shell and the hot bubble contained in it into the diffuse intercloud gas, and the resulting structures. The simulations are continued until the size of the bubble expanding in the intercloud gas becomes approximately one order of magnitude greater than that of the initial bubble at the time of blowout.

Fig. 3. (continuation of Fig. 2); the frames now correspond to the evolution $2.5 \cdot 10^5$, $3 \cdot 10^5$, $3.5 \cdot 10^5$, and $4 \cdot 10^5$ yr after blowout. The area covered by each frame is 36.34 pc x 36.34 pc

3.1.1. O4 star, $d = 1.5 R_S$

Our first numerical simulation describes the expansion of the bubble generated by a O4 star located at $d = 1.5\ R_S$ from the boundary of the molecular cloud. In the initial conditions described in Sect. 2, $R_S \sim 1.5$ pc. We follow the expansion along the first 400,000 years after breakout; the results are shown in Figs. 1 and 2, where the evolution of the values of the density and the thermal pressure are displayed in a logarithmic greyscale on the computational plane which contains the axis of symmetry.

The HII region initially surrounding the star is a thin, compressed shell. Very soon after the shell starts its expansion into the intercloud medium, the shell/bubble boundary follows it. As a consequence, the phase in which the expansion of the HII region into the intercloud medium is driven by the pressure difference between the dense ionized gas and the tenuous intercloud gas is very short, only a few times 10^4 years in our initial conditions, and soon the HII shell as a whole is accelerating outwards pushed by the hot bubble interior. In these conditions, we expect the shell to become Rayleigh-Taylor unstable, and break up in fragments. This is difficult to follow in a 2-D simulation, given that the azimuthal components of the perturbations are not reproduced, and the growth of the instabilities is therefore inhibited as the distance to the axis of symmetry increases. However, near the axis we indeed see that the boundary between the shell and the bubble deforms. Finally, the bubble breaks out of the shell flanked by two denser blobs. This part of the bubble begins a fast expansion into the intercloud medium, which is now a diffuse HII region due to the release of the ionization front as the density of the blown out HII shell decreases.

The dense blobs lag behind the expanding shell, which after 10^5 years has been disrupted by the bubble in other points too, and find themselves surrounded by a hot medium whose pressure decreases with time due to the growth of the bubble. Moreover, the large temperature difference produces a flow of energy into the blobs due to thermal conduction. The combined effect of expansion against the decreasing bubble pressure and evaporation due to thermal conduction ends up by diluting these fragments of the initial shell in the hot bubble interior.

A few shock structures form inside the bubble as the hot gas is accelerated, then shocked, then accelerated again by pressure gradients. In the frame corresponding to the evolution after 10^5 years, three such shocks can be seen. The first one defines the boundary between the free flowing stellar wind and the bubble, and always keeps close to the star along the length of our simulations. The expansion of the bubble in the direction of the intercloud medium creates a pressure gradient which produces a fast stream of hot gas (with typical velocities around 1000 km s^{-1}). When this stream reaches the vicinity of the expanding shell, a second shock is formed, separated from the shell by a

Fig. 4. Same as Figs. 2 and 3, but now depicting the evolution of the thermal pressure.

broad layer of gas at a temperature of $\sim 3 \cdot 10^6$ K and with density $n_H \sim 0.5$ cm^{-3}. The thermal pressure of this hot gas drives the expansion of the shell. In the region where the shell was first disrupted, the expansion of the bubble creates a new pressure gradient which in turn generates a third shock near the blown out shell.

At later times, the overall appearance of the HII region can be separated in: 1) a diffuse component, ionized by the release of the ionization front at blowout, slowly expanding by the factor of ~ 2 of pressure difference with its surrounding neutral medium, but still unaffected by the expanding bubble; 2) a dense but thin HII region surrounding the hot bubble, with some dense knots produced by the instability of the shell at blow out; 3) a compact component, contained in the molecular cloud; and 4) an intermediate density HII region formed by the flow of ionized gas from the compact component into the low density intercloud region. This latter component corresponds to the classical *champagne* flow. The denser knots described above react to the pressure of the hot bubble differently from the rest of the shell and, before they are evaporated by conduction into the bubble interior, they distort the shape of the shell. Although higher resolution and a full 3-D treatment is required to follow their development in detail, these knots are likely to cause some of the ubiquitous filamentary structures seen in HII regions.

Although the bubble blowout rapidly decreases the pressure inside the compact component, which was driving the early expansion of the HII region previously to the blowout, the HII region continues to expand into the molecular cloud all along the time span covered by our simulations. In fact, the expansion rate can be enhanced by the blowout, in spite of the decrease in pressure, as noted by Franco et al. 1994: the flow of ionized gas toward the intercloud region decreases the column density between the ionization front and the star, and more photons are available to ionize fresh gas from the molecular cloud. On the other hand, the stellar wind provides ram pressure inside the compact component, keeping its volume density high. The continued flow of gas out of the compact component maintains a "wall" of moderately density gas which keeps the flow of hot gas weakly collimated during the whole span of our simulations. The importance of this collimating effect is expected to increase as the importance of ionization vs. stellar wind increases (i.e., as the parameter ξ introduced in Sect. 2 decreases), as is confirmed by the simulations in Sect. 3.1.3.

At the end of our simulations, $4 \cdot 10^5$ years after blow out, the shocked stellar wind, mass-loaded by thermal conduction with gas from the compact HII region, falls down to a density of 0.02 cm^{-3} and a temperature of $4 \cdot 10^5$ K before being shocked again inside the bubble. The doubly-shocked gas driving the expansion of the bubble has now a density of 0.15 cm^{-3} and

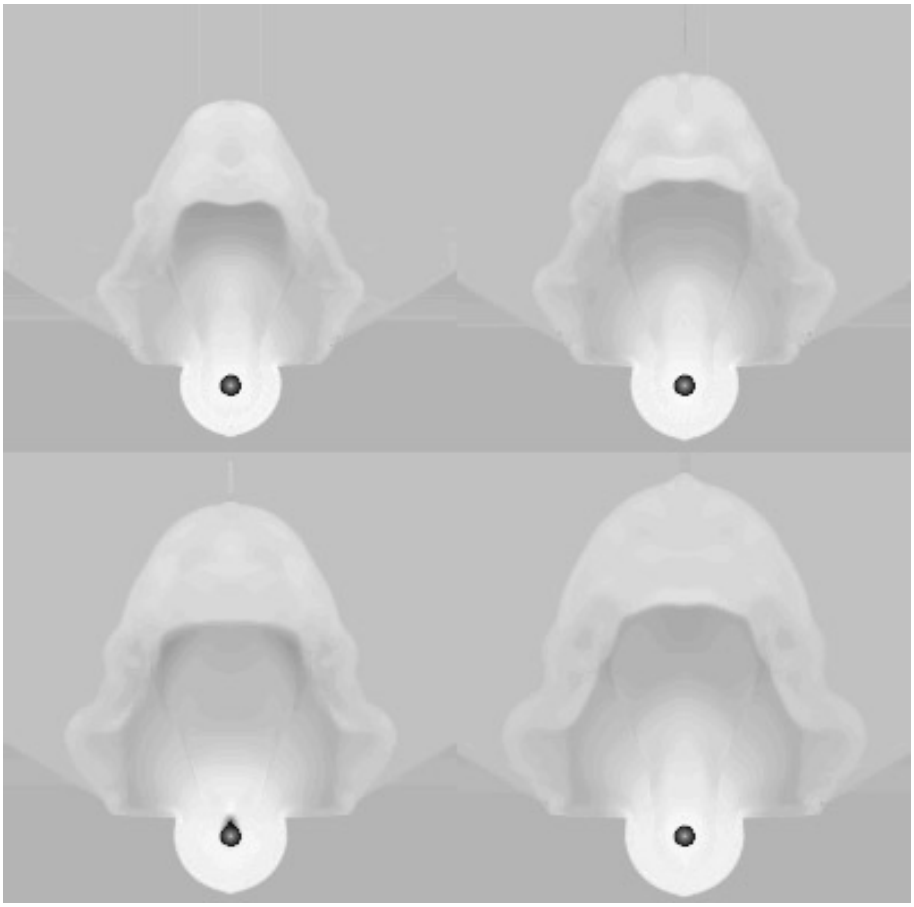

Fig. 5. Continuation of Fig. 4

a temperature of typically 10^6 K, which produces a pressure about 6 times larger than the pressure in the diffuse ionized gas against which it expands. This is to be compared with a pressure ratio exceeding 800 at blow out. The compact component has a density of 120 cm^{-3}, which decreases in the *champagne* flow to 1.2 cm^{-3}. Its expansion against the intercloud medium raises its density at the outer layers to about 6 cm^{-3}, about a factor 2 larger than the density of the diffuse ionized intercloud medium. Typical densities in the new shell of swept-up gas, expanding at a velocity of about 50 km s^{-1}, are of order of 20 cm^{-3}.

3.1.2. O4 star, $d = 3R_S$

We have repeated the calculations with the same stellar parameters, but now placing the star $3R_S$ from the cloud-intercloud boundary. With the data of Table 1, Eq. (11) gives in this case $d \simeq 3$ pc, implying a minimum diameter of the embedding clump of over of 6 pc. This is rather large for a clump of this density (Williams et al. 1995), but still useful for comparison with the case outlined in Sect. 3.1.1. The essential difference in the initial conditions with respect to the $d = 1.5$ case is that the dense shell containing the HII region is more massive, and is expanding more slowly at the time of blow out. The pressure of the hot gas is only $\simeq 50\%$ that of the previously presented case. As a consequence, we may expect the initial HII shell to have a more important rôle in determining the dynamical evolution of the bubble.

The evolution of the density in this case is shown in Fig. 6. The initial evolution is much slower than in the case $d = 1.5$, due to both the smaller pressure from the shocked stellar wind and the larger inertia of the thicker HII layer. After 10^5 years, the expansion of the ionized shell into the intercloud medium is still dominated by its own thermal pressure, rather than by the pressure of the hot gas in the bubble. The expansion does not release the ionization front until a later time.

In the frame showing the density distribution after $2 \cdot 10^5$ years, it can be seen how the hot gas is escaping from the HII shell at different points. The ionization front is released in these points, remaining trapped in others, producing several beams of ionized gas in the intercloud medium. The denser blobs between the shell breakouts are still trapping the ionization front, shielding the gas behind them from the ionizing radiation of the star. This causes a pressure difference between these blobs and the hot gas surrounding them, which tends to further compress regions of high density. This kind of instability has been discussed in detail by Giuliani 1982 and García- Segura & Franco 1996. The azimuthal symmetry imposed in our simulations implies that the high density spikes appearing in the second frame of Fig. 6 are actually rings when they are not in the axis of symmetry, while only the central spike is a real high density column.

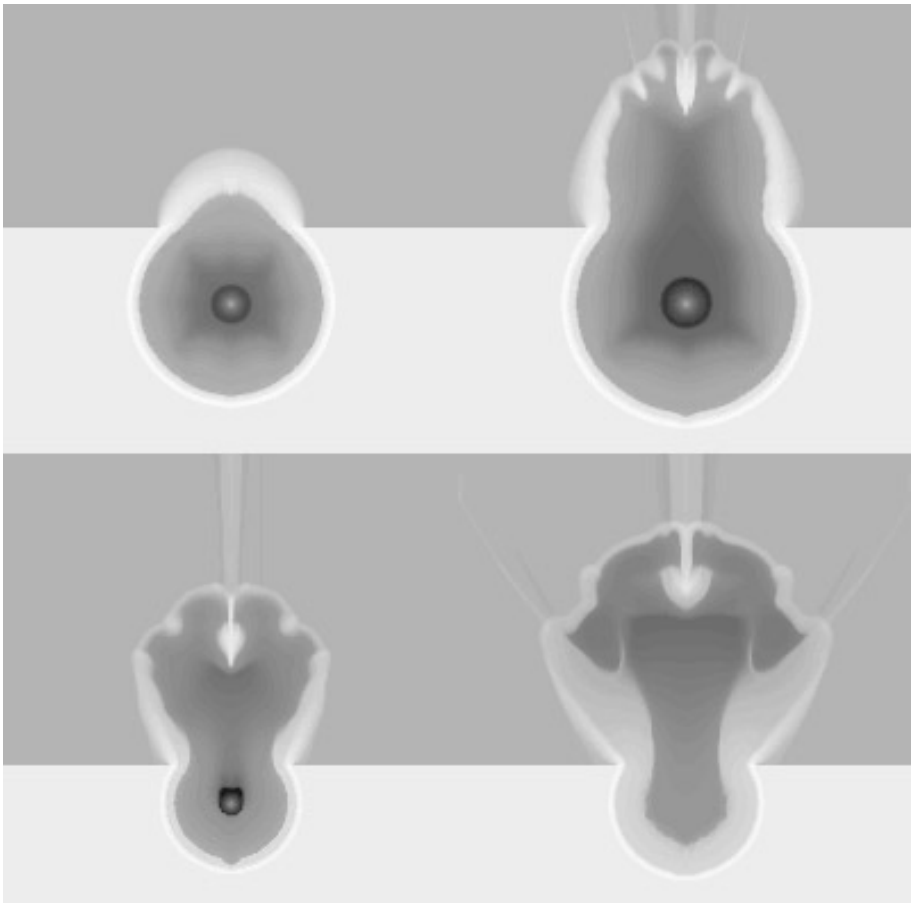

Fig. 6. Evolution of the density in the computational plane for a O4 star located 3 Strömgren radii from the cloud boundary. The frames correspond to the evolution $1 \cdot 10^5$, $2 \cdot 10^5$, $3 \cdot 10^5$, and $4 \cdot 10^5$ years after blowout. The initial size of the computational grid (upper left frame) is 18.17 pc x 18.17 pc. The computational grid has been upscaled by a factor of 2 between the second and the third frame. See Sect. 3.1.2 for a detailed explanation of the different features appearing in these frames.

As a result, the pressure of the hot gas over the dense protrusions produces a greater compression on the central one, which tends to grow much denser than the others. This is a well known feature of 2-D simulations in cylindrical symmetry; see for example the simulations by Różyczka & Tenorio-Tagle 1985a, or Blondin & Lundqvist 1993. Since real instabilities can also grow in the azimuthal direction, it can be expected that dense columns such as the one protruding the expanding bubble along the axis of symmetry will actually appear everywhere in the shell, the cylindrical symmetry actually damping the growth of the off-axis ones. The observed counterpart of these dense columns may be the *elephant trunks* commonly observed in HII regions.

As the bubble develops, its evolution is similar to that shown for the d = 1.5 case. However, a morphological comparison between these two cases after $4 \cdot 10^5$ years of evolution shows clear differences. The *champagne* flow out of the compact component is much more conspicuous in comparison to the hot bubble, and the pressure of the bubble gas is less than 3 times that in the ionized intercloud gas. The temperature in the bubble is below $9 \cdot 10^5$ K in all its volume.

Radiative losses play an important rôle in the differences between the d = 1.5 and d = 3 cases. During the expansion of the bubble in the molecular cloud, the high temperature of the shocked stellar wind produces a high rate of evaporation by thermal conduction, which keeps the density, and therefore the cooling rate inside the bubble, relatively high. In the d = 3 case, the bubble has been kept confined in the compact stage for much longer than in the d = 1.5 case, and its further growth finds greater opposition by the thicker HII layer. Cooling by radiation of the gas inside the bubble along its history is thus much higher in the d = 3 than in the d = 1.5 case, thus reducing the ability of the hot gas to drive the expansion of the bubble. We estimate that the energy lost radiatively since the beginning of the expansion of the bubble amounts to $\sim$ 25 % of the internal energy of the bubble at the time of blow out, as compared to less than 10 % for the case discussed in Sect. 3.1.1. This is mostly due to the greater age of the bubble at the time of blowout for the d = 3 case as compared to the d = 1.5 case (95,000 years and 30,000 years, respectively).

3.1.3. B0 star, $d = 1.5R_S$

The evolution of the density of the gas surrounding a B0 star embedded in a molecular cloud at a distance $1.5R_S$ from its edge is shown in Fig. 7. This case is different from the previously studied ones in that, although ξ is relatively large, the condition $d = 1.5R_S$ implies now that the ionized compact shell is rather thin at the time of blow out, which takes place when the age of the shell is only 13,000 years. As a result, the pressure of

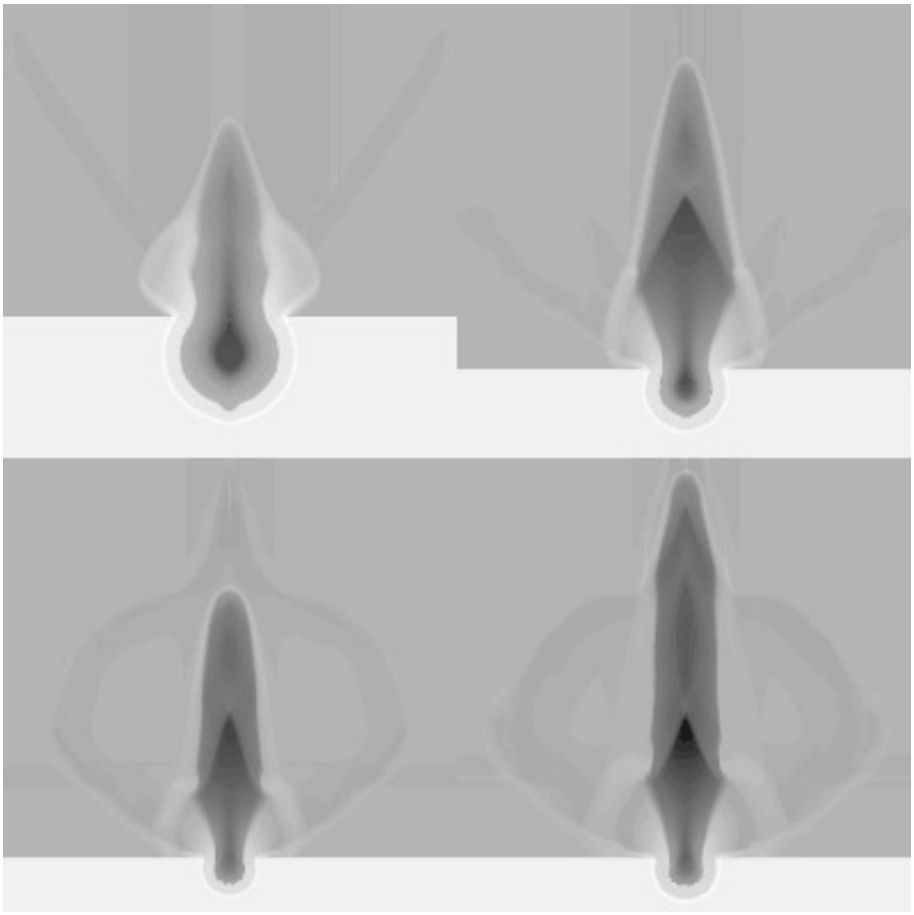

Fig. 7. Evolution of the density in the computational plane for a B0 star located 1.5 Strömgren radii from the cloud boundary. The frames correspond to the evolution $2.5{\cdot}10^4$, $5{\cdot}10^4$, $1{\cdot}10^5$, and $1.4{\cdot}10^5$ years after blowout. The size of the computational grid in the upper left frame is 3.88 pc x 3.88 pc. The computational grid has been upscaled by a factor of 2 between the first and the second frame, and again between the second and the third frame. See Sect. 3.1.3 for a detailed explanation of the different features appearing in these frames.

the hot bubble at blow out is relatively high, 200 times that of the intercloud gas, and the original ionized shell is quickly disrupted.

The combination of a strong pressure discontinuity and a thin shell causes large velocities of the hot gas along the axis of symmetry, and therefore, given the small size of the bubble, large velocity gradients. Such velocity gradients have an important dynamical effect on the expansion: given that, for an adiabatically expanding monatomic gas, the sound speed $c_s \propto \rho^{1/3}$, a linear expansion in the direction z causes the ratio of ram-to-thermal pressures vary as

$$\frac{\partial}{\partial z}\left(\frac{U^2}{c_s^2}\right) = \frac{8}{3}\frac{U}{c_s^2}\frac{\partial U}{\partial z} \qquad (22)$$

where we have assumed a stationary flow, an acceptable approximation given that $(\partial U/\partial z)^{-1}$ is well below the expansion timescal of the bubble. Eq. (22) thus indicates that the large velocity gradients generated by the bubble breakout dramatically decrease the importance of the thermal pressure in front of the ram pressure. In this case, therefore, the expansion of shell of swept-up gas in the intercloud medium is mostly ram-pressure dominated, and takes place predominantly in the z direction. This produces a fairly well collimated flow of hot gas, rather than a bubble. The temperature of the shocked gas at the head of the jet is somewhat below $9 \cdot 10^5$ K, and about half that value along most of the jet length. Fig. 8 shows in detail the distribution of the ratio of the momentum in the z direction to the thermal pressure, comparing a thermal pressure-dominated case (that described in Sect. 3.1.1) with the present one.

In our simulations presented in Sects. 3.1.1 and 3.1.2, the expanding bubble decelerated and became close to pressure equilibrium long before it could overtake the ionization front released into the intercloud medium after blowout, i.e., the Strömgren radius in the diffuse intercloud gas. However, in the case described here the ionization front lies closer to the star, and is overtaken by the jet of hot gas in somewhat more than 10^5 years. This can be clearly seen in the last two frames of Fig. 7, which include the outer boundaries of the diffuse HII region. Only in the direction of the jet, due to the much smaller column density, the ionization front can extend to a large distance from the star. On the other hand, the almost lack of expansion in the directions perpendicular to the jet allows the ionized shell to expand against the diffuse HII region, merging with the outflowing ionized gas from the compact component in the molecular cloud near the base of the shell. At the end of our simulation, 140,000 years after blow out, the diffuse HII region in the intercloud medium, the side walls of the jet, and the outer parts of the *champagne* flow all have densities and pressures within a factor of 2 from each other.

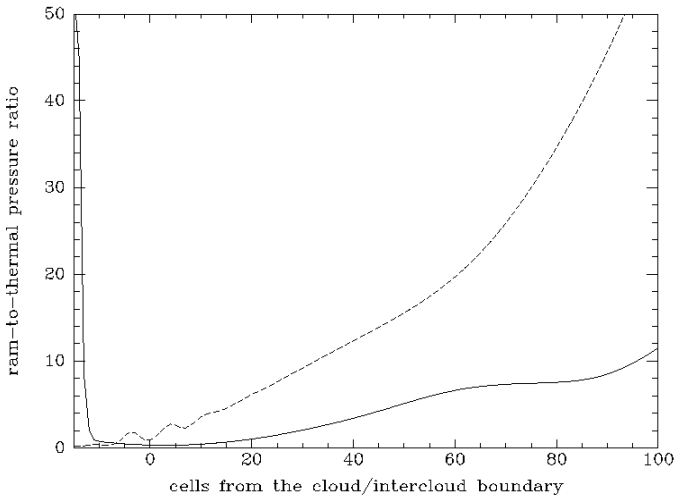

Fig. 8. Distribution of the ram-to-thermal pressure ratio along the axis of symmetry. The dashed line corresponds to the case discussed in Sect. 3.1.3, $2.5 \cdot 10^4$ yr after breakout, and the solid line to the case discussed in Sect. 3.1.1, 10^5 yr after breakout. These times are chosen so that, in both cases, the maximum length of the bubble is approximately equal to the diameter of the compact component.

3.1.4. O4 star, $d = 1.5R_S$, without thermal conduction

Thermal conduction between the hot gas and the warm dense gas in the shell is an essential ingredient in the evolution of wind blown bubbles in the interstellar medium (Weaver et al. 1977; Mac Low & Mc Cray 1988; Van Buren et al. 1990; Shull & Saken 1995). Most of the hot gas inside a bubble comes from material evaporated from its walls, rather than from the stellar mass carried by the stellar wind. It also plays an indirect but fundamental rôle in the cooling of the bubble interior, by determining its density and therefore its radiative cooling rate. For the reasons indicated at the end of Sect. 2.2, the analytical approximation of Weaver et al. 1977 for bubble expansion in a uniform medium is not substantially modified by the inclusion of thermal conduction in the early stages of bubble expansion, given the initial set of parameters with which we are dealing here (although this may not be true in other scenarios; see for example Van Buren et al. 1990). In particular, the internal pressure has a similar evolution in both cases, due to the generally small radiative losses in the bubble interior. However, the temperature inside the bubble varies by nearly two order of magnitude depending on whether only the mass yielded by the star is considered as contributing to the density inside the bubble, or whether the evaporated mass from the shell is also included. This has very important consequences for the high energy emission from the bubble interior, as will be seen in Sect. 3.2.1. On the other hand, we may expect that the dynamical evolution of the bubble after blow out will also be sensitive to the inclusion or not of a thermal conduction term in the energy equation, since the cooling rate becomes important in later evolutionary stages,

To assess the importance of thermal conduction in the dynamical evolution of our model HII regions, we have reproduced the simulations discussed in Sect. 3.1.1, but now without allowing conductive energy exchange between cells, and assuming that the mass initially inside the bubble comes entirely from the stellar wind. The resulting evolution of the density in the computational plane is shown in Fig. 9, which is to be compared to Figs. 2 and 3.

In the initial stages, the larger density contrast between the intercloud medium and the hot gas at blowout enhances the instabilities in the expanding shell, as is visible in the first frame of Fig. 9. The initial expansion is thus faster in this case. As the expansion proceeds, the large thermal pressure pushes the outflow of dense gas from the compact HII region inside the molecular cloud sideways. Later on, a large scale fountain-like flow of hot gas fills the whole bubble: the upward flowing gas undergoes a moderately strong shock (due to its temperature of $\sim 5 \cdot 10^7$ K) well inside the bubble, creating a thick buffer of gas with typical temperatures of $8 \cdot 10^7$ K which expands in all directions. The initial *champagne* flow is pressed against the surface of the molecular cloud. However, gas continues to flow from the compact component, creating a plume of warm ionized gas completely enclosed within the bubble. A part of it is dragged up by the hot gas, tracing its turbulent flow inside the bubble in the last two frames of Fig. 9. In the case without thermal conduction, the *champagne* flow does not play any rôle in collimating the hot bubble gas. The final density of the compact component is 40 % greater than in the case which includes thermal conduction, due to the larger confining pressure generated by the shocked stellar wind. The ionization front expanding into the molecular cloud has nevertheless the same radius in both cases.

3.1.5. O4 star, $d = 1.5R_S$, without stellar wind

Our final simulation corresponds to the classical *champagne* flow scenario, which we now follow using the same parameters as in the cases discussed in Sects. 3.1.1 and 3.1.4, but suppressing the stellar wind. The evolution of the density is presented in Fig. 10. The absence of the hot gas bubble simplifies the dynamics of the gas, which now follows the behaviour outlined by Tenorio-Tagle et al. 1979. The outflow of ionized gas from the compact component reaches velocities of up to 50 km s^{-1} bounded by a broad, weakly shocked layer which expands into the intercloud medium at a velocity of about 20 km s^{-1} in the last frame. The volume affected by the expansion of the HII region after blow out is thus much smaller than in the case including the stellar wind, as could be guessed by comparing the relative sizes of the *champagne* flow and the overall extent of the bubble in the last frame of Fig. 3. The decreased pressure due to the absence of the stellar wind also reduces the expansion rate of the compact ionized component in the molecular cloud; 400,000 years after blowout, its radius is 3.1 pc, as compared to 4.2 pc for the compact HII component in the case including the stellar wind.

We also find differences in the sizes of the regions reached by the *champagne* flows. Although the one in the case with stellar wind can be calculated only roughly, due to its shape being

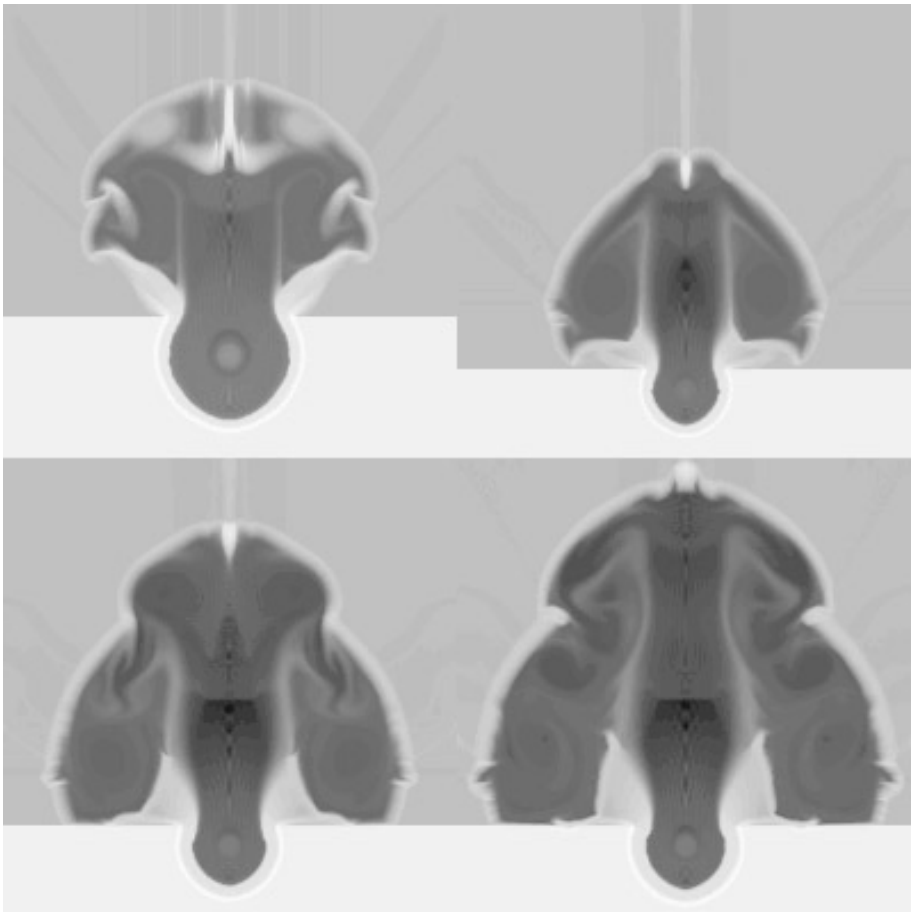

Fig. 9. Evolution of the density in the computational plane for a O4 star located 1.5 Strömgren radii from the cloud boundary. Thermal conduction has been suppressed. The frames correspond to the evolution $1 \cdot 10^5$, $2 \cdot 10^5$, $3 \cdot 10^5$, and $4 \cdot 10^5$ years after blowout. The size of the computational grid in the upper left frame is 18.17 pc x 18.17 pc. The computational grid has been upscaled by a factor of 2 between the first and the second frames. See Sect. 3.1.4 for a detailed explanation of the different features appearing in these frames, and the differences with respect to the case discussed in Sect. 3.1.1.

distorted by the bubble, we estimate it to be about 22 pc, while the outer radius of the expanding flow in the windless case is 15 pc. This is due to the faster initial *champagne* flow in the case including wind, due to the greater pressure (by a factor of nearly 4) at the time of blow out, which produces a faster initial growth. The evolution of the pressure inside the compact component differs remarkably between the two cases, with the expansion of the bubble producing a faster decline. At the end of the time span covered by the simulations, the pressure in the case with stellar wind has dropped below 90 % of the corresponding value in the windless case. The more intense initial outflow, plus the drop in pressure, make the density in the compact component to be 120 cm^{-3} in the case with wind, and twice that value in the windless case at the end of the 400,000 years. The decline of the pressure contributed by the shocked stellar wind inside the compact component is fast after blowout. At late stages, the low density shocked stellar wind quickly leaves the compact component in the direction of the intercloud medium, leaving the stellar wind-contributed pressure in the compact component near its minimum value, given by the ram pressure of the stellar wind ($p_{ram} = \dot{M}_w v_\infty / 4\pi r^2$). The pressure in the compact component thus becomes determined by the balance between the rate at which cloud material is ionized, and the rate at which it can escape in the *champagne* flow.

The different time evolutions of the pressure and the density inside the compact component have an influence on the rate at which material from the cloud is photoionized, as already outlined in Sect. 3.1.1, and ultimately determine the survival time of the cloud after photoionization has set in. Obviously, this also determines the final extent of the *champagne* flow and its morphological relevance with respect to the stellar wind-bolwn bubble. The stellar wind plays only an indirect rôle by regulating the pressure inside the compact component and, to a lesser extent, by evaporating warm ionized gas from the inner walls of the compact HII region into the bubble. The photoionization rate of the cloud can be expected to be sensitive to many parameters, such as the density, the ionizing flux, the degree of clumpiness, or the depth of the ionizing star inside the cloud. Including the stellar wind only adds more free parameters to the problem, without it being likely to change the essential fact that photoionization is the ultimate agent driving the destruction of the cloud. This conclusion stands even if the star explodes as a supernova while still partially embedded in the cloud (Yorke et al. 1989).

3.2. Simulated maps

Observations in different windows of the electromagnetic spectrum permit useful diagnostics on aspects such as the physical

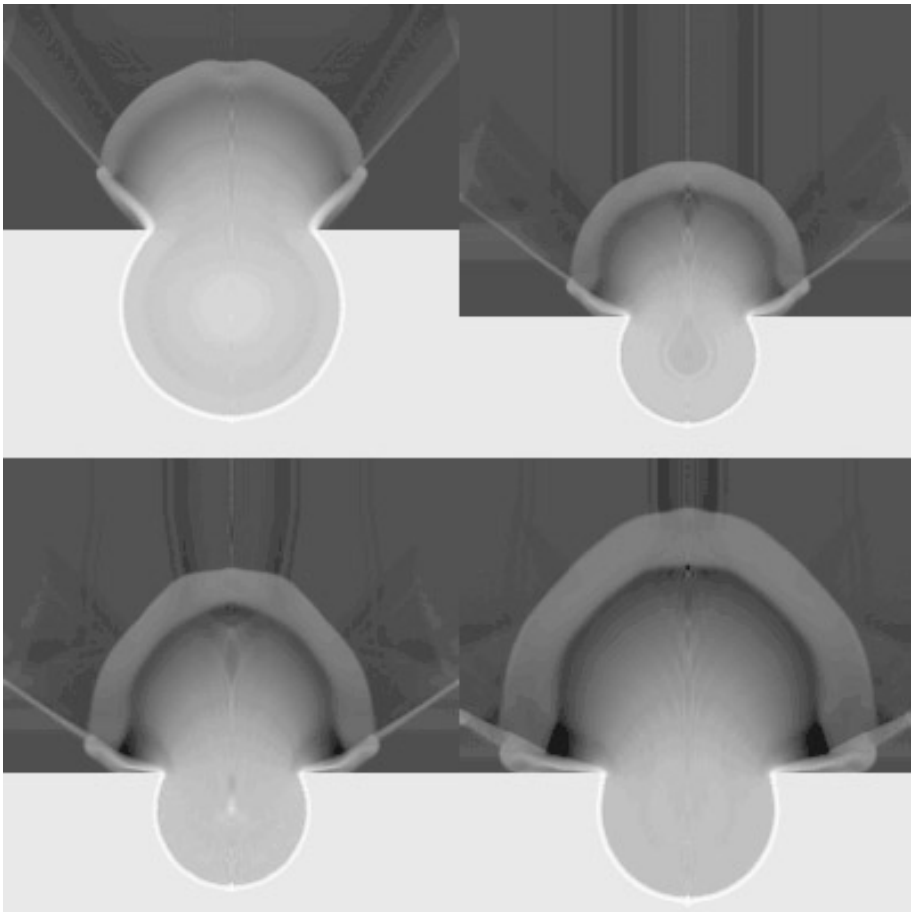

Fig. 10. Evolution of the density in the computational plane for a O4 star located 1.5 Strömgren radii from the cloud boundary. No stellar wind is considered in this case. The initial size of the computational grid (upper left frame) is 9.08 pc x 9.08 pc. The frames correspond to the evolution $1 \cdot 10^5$, $2 \cdot 10^5$, $3 \cdot 10^5$, and $4 \cdot 10^5$ years after blowout. The computational grid has been upscaled by a factor of 2 between the first and the second frames. See Sect. 3.1.5 for a detailed explanation of the different features appearing in these frames, and the differences with respect to the case discussed in Sect. 3.1.1.

conditions of the gas across the HII region, its internal dynamics, the parameters of the exciting star, or the metal abundances. Our simulations allow us to proceed inversely: having calculated the values of physical variables as they evolve in the neighbourhood of a star with a given set of parameters, we can derive simulated maps in different spectral domains. Such simulated maps in visible wavelengths were produced by Yorke et al. 1983, 1984 for the windless *champagne* phase.

Here we present maps of high energy and centimeter emission which probe well differenced components of our model HII regions: the hot gas inside the bubble, and the moderately dense ionized gas properly defining the HII region.

3.2.1. X-ray emission

Recently, HII regions in our Galaxy and the Magellanic Clouds have been extensively observed in X-rays thanks to the information collected by the *Einstein* and ROSAT satellites (see the Introduction for references), and they will surely be a primary target for future missions such as AXAF and XMM. X-ray observations are generally presented in the form of maps of the intensity emitted in different broad bands, allowing one to define a *hardness ratio* primarily related to the temperature of the emitting region. The galactic interstellar medium is relatively transparent to X-ray bands with energies around 1 keV, where intense emission is expected from gas at the temperatures of wind-blown bubbles or young supernova remnants. This makes these observations a very useful tool for the study of both the internal processes of these objects and the galactic structure as traced by them.

The maps of X-ray emission presented here use the curves of integrated cooling efficiency $\mathscr{L}$ in broad bands calculated by Raymond et al. 1976, which include free-free, recombination, and line emission. The emissivity per unit volume is thus $\epsilon = n_H^2 \mathscr{L}$. To directly use the results of Raymond et al. 1976, we have considered two broad bands covered by the ROSAT channels, namely those between 0.53 and 0.87 eV (the "soft" band) and between 0.87 and 1.56 keV (the "hard" band). The effects of interstellar extinction can be noticeable in these bands. Given the low density of the intercloud medium where the bubble expands, extinction of X-rays from most of the bubble volume can be expected to be produced almost entirely in the intervening interstellar medium, unrelated to the HII region. We do not consider this distance-dependent interstellar extinction in our maps. In the case of the X-ray emission produced inside the compact component, however, the line of sight will generally pass through a considerable column of dense gas, unless it is seen nearly pole-on (where pole-on is defined as the situation in which the line of sight is perpendicular to the cloud boundary). We will consider this extinction as internal, in the sense that it is

produced in the molecular cloud + HII region complex. Given typical densities and lenghtscales of our simulations, internal extinction dominates over the interstellar extinction for HII regions located within a few kiloparsecs from the Sun. In order to take into account extinction in our calculations, we have used the cross section values of Morrison & McCammon 1983. An accurate evaluation of attenuated X-ray emission maps would require to consider the variation of the extinction over the broad bands considered, as well as the precise spectral energy distribution of each X-ray emitting volume. To simplify, we have used instead the value of the extinction averaged over the wavelength interval covered by each band. We have not considered in our maps the contribution of the X-ray emission arising from the immediate neighbourhood of the exciting star itself (Chlebowski & Garmany 1991).

Our results are presented in Fig. 11 for the case discussed in Sect. 3.1.1. The bubble is shown from two different vantage points, forming angles of 20^0 and 70^0 with the axis of symmetry, at the end of the interval covered by our simulations. Fig. 11 displays the integrated emission in the soft band and the hardness ratio H defined as

$$H = \frac{L_{hard} - L_{soft}}{L_{hard} + L_{soft}} \tag{23}$$

where L is the luminosity in the corresponding band.

A characteristic feature of the dynamics of the hot gas in our models is the production of two peaks in the X-ray luminosity, which become more detached as we proceed to higher energies. Such a distribution is reminiscent of that observed in some HII regions such as RCW 49 (Belloni & Mereghetti 1994). We refer to those peaks as the *compact* and the *extended* components, arising from the vicinity of the star and from the bubble expanding in the intercloud medium, respectively. As could be expected, the most intense X-ray emission comes from the compact component, both in soft and hard rays. However, when the HII region is seen at a high angle from the axis of symmetry, the soft radiation from the compact component is greatly atenuated by the intervening dense gas. The effects of this can be appreciated in the bottom left panel of Fig. 11, where the spot of large hardness ratio (nearly 1) lies near the position of the star, but further inside the cloud. This is almost entirely due to extinction, rather than to the intrinsic hardness of the radiation in that region; the more pole-on view in the right side panels minimizes the effects of the extinction. The intrinsic soft X-ray emission from the compact component has a peak approximately 40 times more intense than that of the extended component. The intrinsic hardness ratio reaches a maximum of -0.46 in the compact component and -0.78 in the extended one, dropping to -0.93 in the *chimney* connecting the compact component with the shocked gas in the extended one.

3.2.2. Free-free emission

Centimeter-wavelength observations are widely used in studies of HII in regions (see e.g. Spitzer 1978, Scheffler & Elsässer 1987, Gordon 1987, Osterbrock 1989, for introductions to the field). The continuum emission is dominated by thermal bremsstrahlung, and high-level transitions of hydrogen and helium (the so-called recombination lines) are abundant in this wavelength range. The high resolution presently available at these wavelengths in velocity and, with aperture synthesis, also in position, make these observations a fundamental tool for the study of the physical conditions and internal kinematics of HII regions.

We have produced simulated maps of free-free continuum emission in the centimeter wavelengths where the HII region is optically thin. We estimate the continuum optical depth using the approximation of Altenhoff et al. 1960:

$$\tau_c \simeq 0.08235 \nu^{-2.1} T_e^{-1.35} EM \tag{24}$$

where ν is the frequency in GHz, T_e is the electron temperature in K, and EM is the emission measure in cm^{-6} pc. For the set of conditions of our simulations, the maximum value of τ_c reaches only $\tau_c \simeq 10^{-3}$ in the compact component for the commonly used wavelength λ = 6 cm, being much smaller elsewhere. The intensity I depicted in our maps is the emissivity integrated along the line of sight l:

$$I \propto \int_l n_H^2 x^2 T^{-0.35}\, dl \tag{25}$$

where x is the ionization fraction. The proportionality factor depends weakly on the frequency of the observations. The weak dependence of Eq. (25) also on the temperature makes our maps to trace essentially the emission measure of the ionized gas.

The results are presented in Fig. 12. Like for the maps of X-ray emission, the HII region is shown from two vantage points, with lines of sight forming angles of 20^0 and 70^0 with the axis of symmetry. The figures depict the case discussed in Sect. 3.1.1 at the end of the period covered by the simulations. For the sake of comparison, a free-free continuum map is also shown for the windless case in Fig. 12.

Free-free emission is dominated by the compact component, and limb brightening can be appreciated in the extended component both in the cases with and without wind. In the case with wind, this is due simply to the fact that the HII region is the envelope of the bubble of hot gas, while in the windless case the limb brightening outlines the weak shock caused by the expansion of the ionized gas in the cloud and intercloud medium. The compact component is also limb-brightened in the case with wind, but not in the windless case, in which the intensity decreases by a factor of 2.2 going from the center to the limb (although this is difficult to appreciate in Fig. 12, due to its dynamic range of two orders of magnitude to account for the differences between the compact and the extended components). In both cases, there is an extended halo of emission produced in the intercloud medium, ionized by the release of the ionization front shortly after the bubble blowout. The actual intensity of this halo depends on whether the diffuse HII region extending in the intercloud medium is density or ionization bounded. For our O4 star, the Stromgren sphere in the intercloud medium would extend out to a distance of nearly 50 pc from the star and, assuming it to be hemispherical, would contain about $2 \cdot 10^4$ M$_\odot$

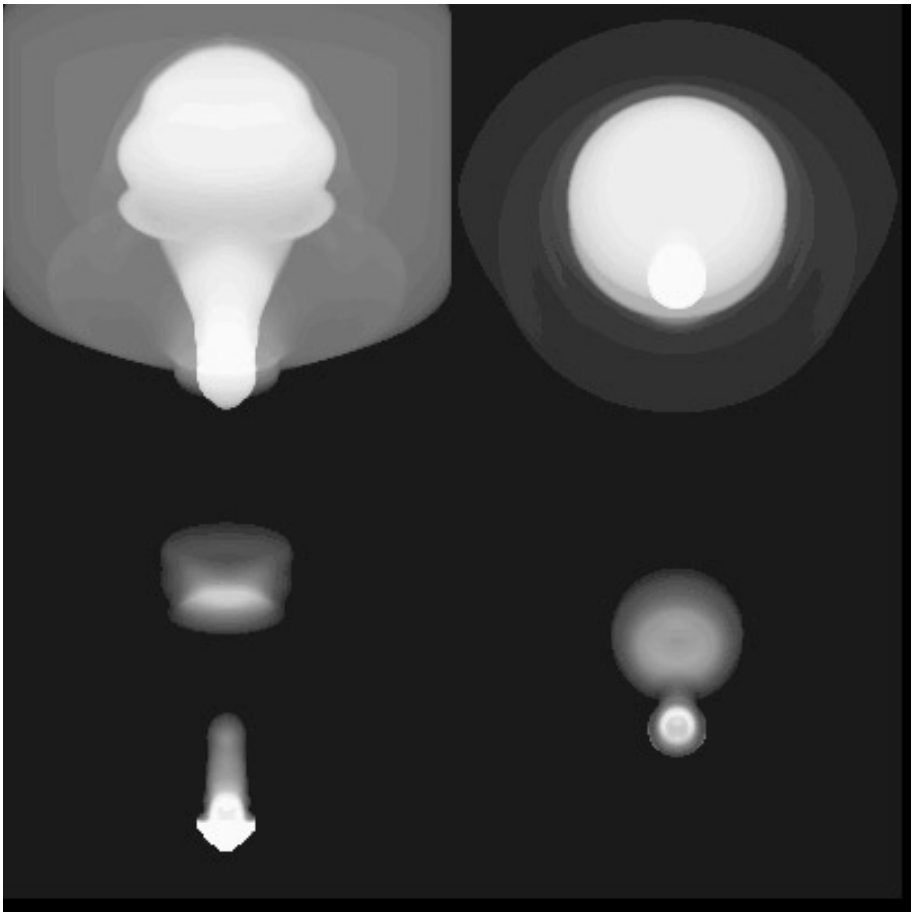

Fig. 11. Simulated maps of soft X-ray emission (*upper panels*) and hardness ratio (*lower panels*) corresponding to the case described in Sect. 3.1.1, after $4 \cdot 10^5$ years of evolution. The panels on the left correspond to a line of sight forming an angle of 70^0 with the axis of symmetry, and those on the right, to an angle of 20^0. The area displayed in each panel is 36.34 pc x 36.34 pc. See Sect. 3.2.1 for a detailed discussion.

of gas. This is of order of the total HI contents of some typical giant molecular clouds in the solar neighbourhood (Blitz 1993), so the most likely scenario for this diffuse component is the density bounded one. Therefore, in our simulated maps we have not added the contribution of diffuse ionized gas lying between the limits of our computational grid and the outermost ionization front.

In spite of the differences discussed in Sect. 3.1.5, the peak intensities in the compact and extended components are similar in the cases with and without wind in the evolutionary stage presented here. In the compact component, the lower density in the case with wind is compensated by its larger extent, while in the extended component the higher density and larger size of the expanding shell is compensated by its thinness. This leaves its peak emission measure similar to that of the weakly shocked outer boundary of the *champagne* flow.

3.2.3. Low frequency recombination line emission

Our last set of maps show the ratio of intensities between a hydrogen recombination line and the underlying free-free continuum at a fixed frequency. The choice of a single frequency, rather than the value integrated over the line, is intended to put emphasis on the kinematics, rather than on the physical conditions of the emitting gas.

To calculate the line to continuum intensity ratio at a given frequency ν, $I_L(\nu)/I_c$, we first consider its LTE value:

$$\frac{I_L(\nu)}{I_c} = A \frac{\int_l n_H^2 x^2 T_e^{-1.5} \Phi(\nu) \exp(\frac{1.579 \cdot 10^5}{n^2 T_e})\, dl}{\int_l n_H^2 x^2 T_e^{-0.35}\, dl} \qquad (26)$$

where n is the principal quantum number of the final state of the transition, $\Phi(\nu)$ is the normalized line profile function, and A depends on ν, n, the difference between levels in the transition Δn, the oscillator strength of the transition, and the helium to hydrogen ratio. In the centimeter range considered here lie many of the α recombination lines (Δn = 1) with values of n around 100; therefore, the exponential term in the numerator of Eq. (26) has a value very close to unity across the ionized region.

Eq. (26) should however be modified in case of NLTE. For transitions to values of n around 100, as those considered here, the population factors b_n describing the departure from LTE are expected to be well below unity for all the range of physical conditions covered by our simulations (Sejnowski & Hjellming 1969), so we cannot directly apply Eq. (26). For NLTE in optically thin conditions ($\tau_c \ll 1$, which applies here as discussed above), the line intensity is modified (Gordon 1987) by:

$$I_L(\nu) \simeq I_L^*(\nu) b_{n'} (1 - \frac{\tau_c}{2} \gamma) \qquad (27)$$

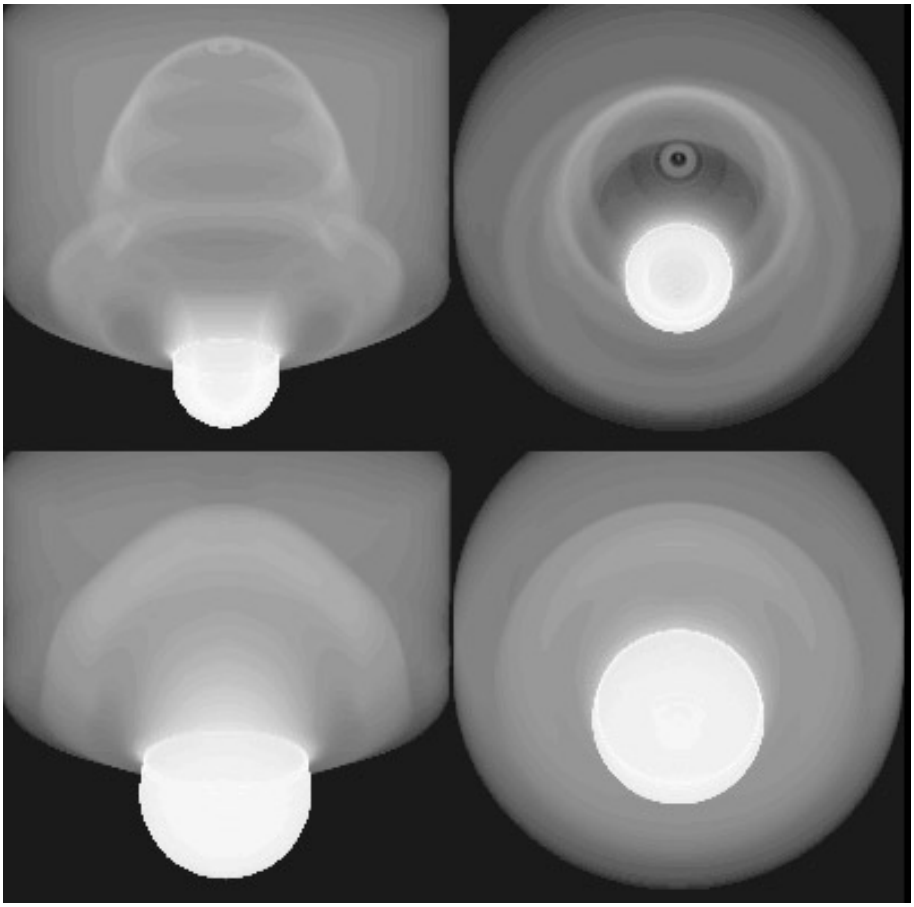

Fig. 12. Simulated maps of free-free emission, for the cases with (*upper panels*) and without (*lower panels*) stellar wind. The initial parameters are those described in Sect. 3.1.1, and the frames shown here correspond to $4 \cdot 10^5$ years of evolution. The panels on the left correspond to a line of sight forming an angle of 70^0 with the axis of symmetry, and those on the right, to an angle of 20^0. The area displayed in each panel is 36.34 pc x 36.34 pc. See Sect. 3.2.2 for a detailed discussion.

where $I_L^*(\nu)$ is the line intensity in LTE, n' is the departure level of the transition, and γ is

$$\gamma = 1 - \frac{d \ln b_{n'}}{dn} \Delta n \frac{kT_e}{h\nu} \tag{28}$$

Curves giving the value of $d \ln b_{n'}/dn$ as a function of n can be found in Sejnowski & Hjellming 1969 for typical conditions in HII regions, ranging from diffuse to compact. For α transitions to levels with $n \simeq 100$ at frequencies around 5 GHz (6 cm), we find $\gamma \sim -80$, which multiplied by our estimate of the maximum value of τ_c in our simulations, $\tau_c \sim 10^{-3}$, makes the factor in parentheses in Eq. (26) deviate from unity by not more than about 4%. In good approximation, therefore, our line intensities are reduced with respect to the LTE values by a factor b'_n. This factor is somewhat dependent on the temperature and density of the medium but, from Figs. 2 and 3 of Sejnowski & Hjellming 1969, we find that $b_{n'}$ lies always between 0.7 and 0.8 for the conditions found in our simulations. Taking all this into account, we can use Eq. (26) to produce our maps, simply reducing it by a factor 0.75, without introducing an error greater than 10 %. We have thus engulfed this factor in the constant A and, since the latter depends on the precise characteristics of the transitions to be considered, we have left our maps of line to continuum ratio uncalibrated for the sake of generality.

For the line profile function $\Phi(\nu)$ we have used a Gaussian shape, considering only thermal width, Doppler shifted by the bulk motion of the emitting volume. Writing it explicitly as a function of the macroscopic LSR velocity v rather than the frequency,

$$\Phi(v) = \frac{1}{\sqrt{2\pi}\sigma} \exp(-\frac{v^2 m_H}{2kT}) \tag{29}$$

with

$$\sigma = \sqrt{\frac{kT\nu^2}{c^2 m_H}} \tag{30}$$

m_H being the hydrogen atom mass. For α transitions to levels of $n \simeq 100$ in the range of densities found in our simulations, thermal pressure broadening increases the line width over the thermal component by only a 2 % at most (Brocklehurst & Seaton 1972), and we have not considered it here.

The results are presented in Fig. 13. The cases considered are the same as for Figs. 11 and 12. The upper panels are centered at a radial velocity of 30 km s^{-1} away from the observer, while the bottom ones are centered at the same velocity but with opposite sign. The grey scales in Fig. 13 are adjusted to cover the appropriate dynamic range for each panel, i.e., a given intensity of grey does not correspond to the same value of the line-to-continuum ratio in all the panels.

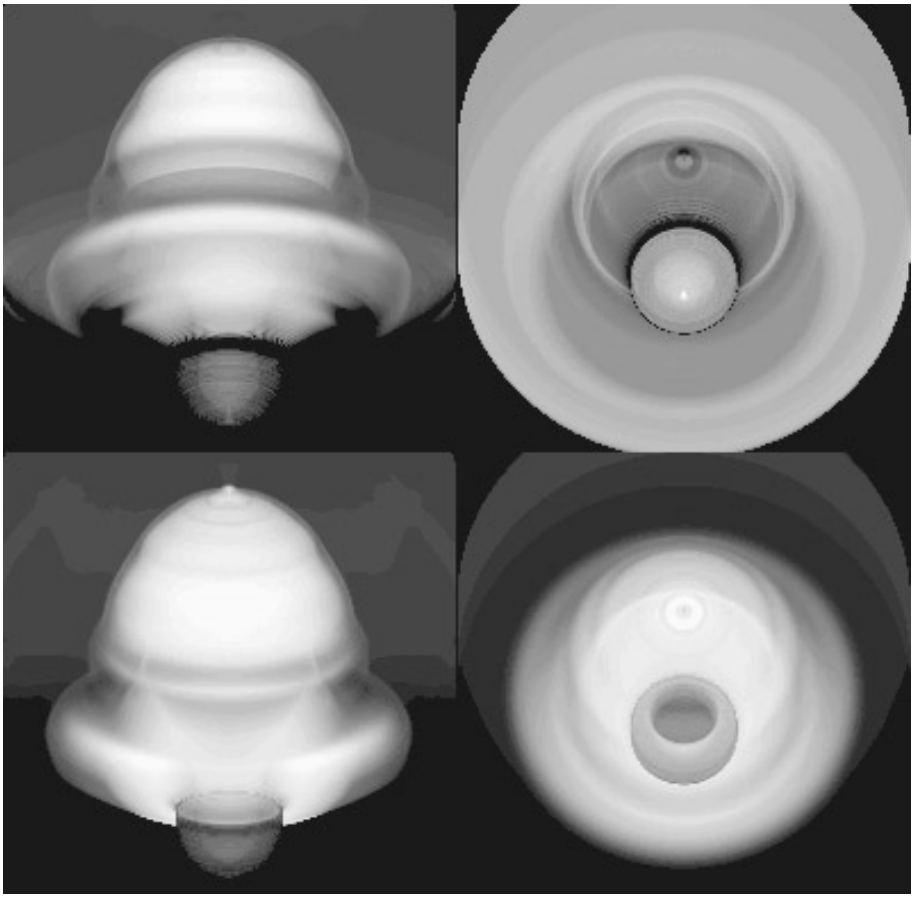

Fig. 13. Simulated maps of recombination line to free-free emission, for velocities of 30 km s^{-1} away (*upper panels*) and towards (*lower panels*) the observer. The initial parameters are those described in Sect. 3.1.1, and the frames shown here correspond to $4 \cdot 10^5$ years of evolution. The panels on the left correspond to a line of sight forming an angle of 70^0 with the axis of symmetry, and those on the right, to an angle of 20^0. The area displayed in each panel is 36.34 pc x 36.34 pc. See Sect. 3.2.3 for a detailed discussion.

As can be expected, the aspect of these *velocity* maps strongly depends on the angle between the axis of symmetry and the line of sight. In the nearly edge-on view displayed in the upper left panel, the brightest areas correspond to the far side of the expanding shell receding from the observer. In the upper right panel, since the bulk of the material is moving towards the observer, the ratio remains very small over the whole area, and is in fact dominated by the wings of the nearly zero-velocity gas of the diffuse ionized intercloud medium. In the bottom panels, the wings of the lines produced in the parts of the expanding shell approaching the observer dominate (this is, most of the gas in the nearly pole-on view of the last panel). The gas in the compact component also expands, but much more slowly than the 30 km s^{-1} at which our maps are centered. The high density of the compact component provides a bright continuum background to the line emission from the shell in the regions that are seen projected against it. This is the reason why its position is marked by a dark circle in the bottom panels of Fig. 13.

A common feature to the cases with and without wind is that most of the high density gas is contained in the compact component and the *champagne* flow. These regions are thus those which dominate the emission measure integrated over the whole area of the HII region; as a consequence, one should not expect appreciable differences in the integrated line profiles between the cases with and without wind in observations of distant, unresolved HII regions. To illustrate this point, we have integrated the line profiles $I_L(\nu)$ over the whole projected area of the simulation seen pole-on. This should be the most favourable case to make out the differences between the cases with and without wind. The results show that differences in the integrated line profile can be noticed only in the high velocity wings, primarily the blueshifted one. Moreover, if the lines of light elements are considered, these differences are almost completely masked by the thermal wings of the much more intense emission from the gas moving at slower velocities. To enhance the differences between both cases, we present in Fig. 14 the results of the calculations with the thermal linewidth used in Eq. (29) reduced by a factor of 100. Note that the scale in Fig. 14 is logarithmic, i.e., significant differences begin to appear only at emission levels about four orders of magnitude fainter than the peak. The main departure from the broad, asymmetric profile of the windless *champagne* phase (which is clearly different from the typical profiles produced by expanding shells; Tenorio-Tagle et al. 1996) is produced at velocities larger than 40 km s^{-1}, arising in the expanding shell. Larger velocities at very low emission levels come from the boundary layers between the shell and the hot gas. This low level emission probably has an important contribution from numerical effects, due to the sharp gradients in density, temperature and velocity in these layers, which are smoothed over a few computational cells.

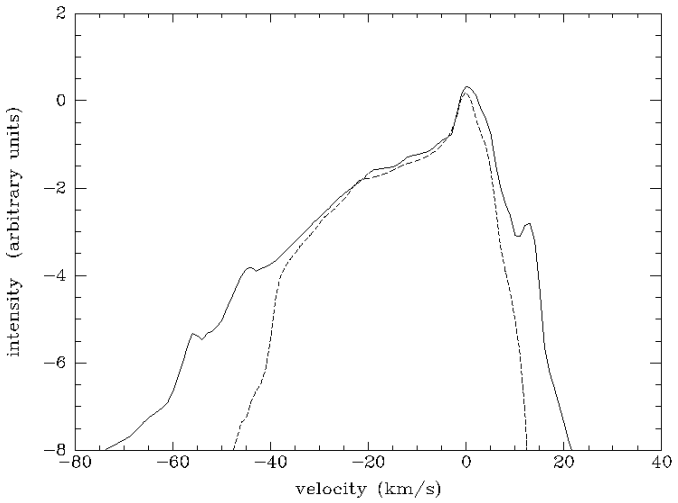

Fig. 14. Emission line profile integrated over the whole area of a HII region seen pole-on. The solid line corresponds to the case described in Sect. 3.1.1, and the dashed line, to that of Sect. 3.1.5, both of them at an age of $4 \cdot 10^5$ yr.

4. Conclusions

Stellar winds are an essential ingredient in understanding the dynamical evolution of HII regions and in interpreting observations carried out in different spectral domains. The kinematic structure produced by the expansion of the bubble of shocked stellar wind after blowing out of the parental molecular cloud is sensibly different from that obtained by considering only the photoionizing flux of the central star, leading to a much larger volume affected by the expansion of the wind-driven bubble. Theoretical maps of X-ray emission, free-free continuum emission at long wavelengths, and line-to-continuum ratios at a fixed frequency have been presented and interpreted in terms of the dynamical evolution of the gas, followed by means of 2-D axisymmetric numerical simulations.

The main differences between the cases with and without wind take place in the expansion of the hot bubble in the intercloud medium. Features of the classical *champagne* model, such as the expansion of the compact component in the parental molecular cloud and the outflow of dense, ionized gas (the *champagne* flow) into the intercloud medium, are not substantially changed when including the stellar wind. The wind has an indirect influence in the destruction of the molecular cloud by keeping a higher pressure inside the compact component than in the windless case. However, this higher pressure produces effects going in different directions, as explained in Sect. 3.1.5, and although the net result in the cases explored here is a somewhat faster rate of photoionization of fresh dense cloud material, the differences introduced by the stellar wind are not dramatic as far as the destruction of the cloud is concerned. On the other hand, as discussed in 3.2.3 and shown in Fig. 14, there is almost no difference in the integrated line profiles between the cases with and without wind. This is a direct consequence of the fact that most of the high density ionized gas is contained in the compact component and the *champagne* flow.

We have carried out an obviously very limited exploration of possible parameters which define the initial conditions of the problem. Even so, it is clear from our results that dramatic variations arise in the dynamical evolution from changing the energetic output characteristics of the exciting star, its distance to the cloud-intercloud boundary, or the physical ingredients included in the simulations, such as thermal conduction. Moreover, the simulated maps presented here show the influence of factors such as the orientation of the HII region with respect to the line of sight or the extinction inside the HII region itself. This illustrates the importance of a proper choice of the input parameters and the viewing geometry when interpreting real observations of HII regions.

Acknowledgements. Valuable comments from Dr. Jordi Torra at different stages of this work, and a careful reading of the manuscript by Dr. Lex Kaper, are gratefully acknowledged. Comments of the referee, Dr. Guillermo Tenorio-Tagle, produced significant improvements in the paper. I also wish to thank the patience and understanding of my colleagues at the University of Barcelona and the European Southern Observatory during the heavy CPU load required by the calculations presented here.

References

Altenhoff, W., Mezger, P.G., Wendker, H., Westerhout, G., 1960, Veröff. Sternwarte Bonn, 59, 48
Arthur, S.J., Henney, W.J., 1996, ApJ, 457, 752
Belloni, T., Mereghetti, S., 1994, A&A 286, 935
Beltrametti, M., Tenorio-Tagle, G., Yorke, H.W., 1982, A&A, 112, 1
Bisnovatyi-Kogan, G.S., Silich, S.A., 1995, Rev. Mod. Phys. 67, 661
Black, J.H., 1987, in "Physical processes in the interstellar medium", ed. H.A. Thronson, D.J. Hollenbach, D. Reidel Publ. Co.
Blitz, L., 1993, in "Protostars and Planets III", eds. E.H. Levy & J.I. Lunine, Univ. of Arizona Press
Blondin, J.M., Lundqvist, P., 1993, ApJ, 405, 337
Bodenheimer, P., Tenorio-Tagle, G., Yorke, H.W., 1979, ApJ 233, 85
Brocklehurst, M., Seaton, M.J., 1972, MNRAS, 157, 179
Bruhweiler, F.C., Gull, T.R., Kafatos, M., Sofia, S., 1980, ApJ, 238, L27
Chlebowski, T., Garmany, C.D., 1991, ApJ, 368, 241
Chu, Y.-H., 1994, in "The soft X-ray cosmos", eds. E.M., Schlegel & R. Petre, American Institute of Physics
Chu, Y.-H., Mac Low, M.M., 1990, ApJ, 365, 510
Cowie, L.L., McKee, C.F., 1977, ApJ, 211, 135
Dalgarno, A., McCray, R., 1972, ARA&A, 10, 375
Dyson, J.E., Williams, D.A., 1980, "The physics of the interstellar medium", Manchester Univ. Press
Franco, J., Shore, S.N., Tenorio-Tagle, G., 1994, ApJ, 436, 795
Franco, J., Tenorio- Tagle, G., Bodenheimer, P., 1990, ApJ, 349, 126
Gaetz, T.J., Salpeter, E.E., 1983, ApJS, 52, 155
García-Segura, G., Franco, J., 1996, ApJ, 469, 171
Giuliani, J.L., 1982, ApJ, 256, 624
Gómez, J.F., Torrelles, J.M., Tapia, M., Gómez, Y., Rodríguez, L.F., Roth, M., Ho, P.T.P., 1993, ApJ, 409, 269
Gordon, M.A., 1988, "Galactic and extragalactic radio astronomy", eds. G.L. Verschuur & K.I. Kellerman, Springer-Verlag

Hollenbach, D.J., Johnstone, D., Lizano, S., Shu, F., 1994, ApJ, 428, 654
Kaper, L., Van Loon, J.T., Augusteijn, T., Goudfrooij, P., Patat, F., Waters, L.B.F.M, Zijlstra, A.A., 1997, ApJ, 475, L37
Keto, E.R., Welch, W.J., Reid, M.J., Ho, P.T.P., 1995, ApJ, 444, 765
Koo, B.-C, Kim, K.-T., Lee, H.-G, Yun, M.-S., Ho, P.T.P., 1996, ApJ, 456, 662
Leitherer, C., Robert, C., Drissen, L., 1992, ApJ 401, 596
Mac Low, M.-M., McCray, R., 1988, ApJ, 324, 776
Mac Low, M.-M., McCray, R., Normal, M.L., 1989, ApJ, 337, 141
Mac Low, M.-M., Van Buren, D., Wood, D.O.S., Churchwell, E., 1991, ApJ 369, 395
Maeder, A., Meynet, G., 1987, A&A, 182, 243
Magnier, E.A., Chu, Y.-H., Points, S.D., Hwang, U., Smith, R.C., 1996, ApJ, 464, 829
Malin, D., 1993, "A view of the Universe", Cambridge Univ. Press
Monaghan, J.J., 1992, ARA&A, 30, 543
Morrison, R., McCammon, D., 1983, ApJ, 270, 119
Norci, L., Oegelman, H., 1995, A&A, 302, 879
Osterbrock, D.E., 1989, "Astrophysics of gaseous nebulae and active galactic nuclei", Univ. Science Books
Raymond, J.C., Cox, D.P., Smith, B.W., 1976, ApJ, 204, 290
Rodríguez- Gaspar, J.A., Tenorio-Tagle, G., Franco, J., 1995, ApJ, 451, 210
Różyczka, M., Tenorio-Tagle, G., 1985a, A&A, 147, 209
Różyczka, M., Tenorio-Tagle, G., 1985b, A&A, 147, 220
Russeil, D., Georgelin, Y.M., Georgelin, Y.P., Le Coarer, E., Marcelin, M., 1995, A&AS, 114, 557
Schaller, G., Schaerer, D., Meynet, G., Maeder, A., 1992, A&AS, 96, 269
Scheffler, H., Elsässer, H., 1987, "Physics of the Galaxy and the interstellar medium", Springer-Verlag.
Sejnowski, T.J., Hjellming, R.M., 1969, ApJ, 156, 915
Shu, F.H., 1993, "The physics of astrophysics", vol II, Univ. Science Books.
Shull, J.M., Saken, J.M., 1995, ApJ, 444, 663
Spitzer, L.A., 1978, "Physical processes in the interstellar medium", Wiley-Interscience
Tenorio-Tagle, G., 1979, A&A 71, 59
Tenorio-Tagle, G., 1982, in "Regions of recent star formation", eds. R.S. Roger and P.E. Dewdney, D. Reidel Publ. Co.
Tenorio-Tagle, G., Bedijn, P.J., 1982, A&A, 115, 207
Tenorio-Tagle, G., Yorke, H.W., Bodenheimer, P., 1979, A&A 80, 110
Tenorio-Tagle, G., Bodenheimer, P., 1988, ARA&A 26, 145
Tenorio-Tagle, G., Beltrametti, M., Bodenheimer, P. Yorke, H.W., 1982, A&A, 112, 104
Tenorio-Tagle, G., Muñoz- Tuñón, C., Cid-Fernandez, R., 1996, ApJ, 456, 264.
Van Buren, D., Mac Low, M.-M., Wood, D.O.S., Churchwell, E., 1990, ApJ 353, 570
Van Buren, D., Mac Low, M.-M., 1992, ApJ, 394, 534
Van Buren, D., Noriega-Crespo, A., Dgani, R., 1995, AJ, 100, 2914
Wang, Q., Helfand, D.J., 1991, ApJ, 373, 497
Weaver, R., McCray, R., Castor, J., Shapiro, P., Moore, R., 1977, ApJ, 218, 377
Wilcots, E.M., 1994, AJ, 107, 1338
Williams, J.P., Blitz, L., Stark, A.A., 1995, ApJ, 451, 252
Yorke, H.W., 1986, ARA&A 24, 49
Yorke, H.W., Tenorio-Tagle, G., Bodenheimer, P., 1983, A&A, 127, 313
Yorke, H.W., Tenorio-Tagle, G., Bodenheimer, P., 1984, A&A, 138, 325
Yorke, H.W., Tenorio-Tagle, G., Bodenheimer, P., Różyczka, M., 1989, A&A, 216, 207.

This article was processed by the author using Springer-Verlag LaTeX A&A style file *L-AA* version 3.